Prototype GaAs X-ray detector and preamplifier electronics for a deep seabed mineral XRF spectrometer

Article (Published Version)

Received: 22 May 2017 | Revised: 14 September 2017 | Accepted: 4 October 2017

DOI: 10.1002/xrs.2818

RESEARCH ARTICLE

WILEY

Prototype GaAs X-ray detector and preamplifier electronics for a deep seabed mineral XRF spectrometer

G. Lioliou | A.M. Barnett

Space Research Group, Sch. of Engineering and Informatics, University of Sussex, Falmer, Brighton BN1 9QT, UK

Correspondence
G. Lioliou, Space Research Group, Sch. of Engineering and Informatics, University of Sussex, Falmer, Brighton, BN1 9QT, UK.
Email: g.lioliou@sussex.ac.uk

Funding information
Science and Technology Facilities Council, Grant/Award Number: ST/M004635/1 and ST/P001815/1; Leverhulme Trust; University of Sussex

Work towards developing a prototype GaAs based X-ray fluorescence spectrometer focusing on the detector-preamplifier system for in situ characterisation of deep seabed minerals is presented. Such an instrument could be useful for marine geology and provide insight into hydrothermal processes. It would also be beneficial for deep sea mining applications. The GaAs photodiode was electrically characterised at 4 °C (ambient seawater temperature) and 33 °C. A system energy resolution (full width at half maximum) at 5.9 keV of 580 eV at 4°C, limited by the dielectric noise, broadening to 680 eV at 33°C, was recorded. The spectral performance of the system was characterised across the energy range 4.95 keV to 21.17 keV, at 33°C, using high-purity X-ray fluorescence calibration samples excited by a Mo target X-ray tube. The charge output from the system was found to be linear with incident photon energy. The energy resolution was found to broaden from 695 eV at 4.95 keV to 735 eV at 21.17 keV, attributed to the increasing Fano noise with energy. The same X-ray tube was used to fluoresce an unprepared manganese nodule (revealing the presence of Mn, Fe, Ni, Cu, Zn, Pb, Sr, and Mo) and a black smoker hydrothermal vent sample (containing Fe, Co, Ni, Cu, Zn, Pb, and Mo). Such a spectrometer may also find use in future space missions to study the hydrothermal vents that are believed to exist in the oceans of Jupiter's moon Europa.

1 | INTRODUCTION

In recent years, there has been renewed interest in deep ocean exploration for economic as well as scientific reasons. Economic interest in the seabed is motivated by the availability of valuable minerals in the deep ocean.[1] At present, elemental characterisation of seabed mineral deposits requires samples to be retrieved and transported to either a surface vessel or to shore.[2] The development of instrumentation for in situ elemental analysis (e.g., X-ray fluorescence spectrometry, XRF) in the ocean would revolutionise scientifically motivated and economically motivated surveying and prospecting. A remotely operated vehicle equipped with an XRF spectrometer or neutron activation analysis package has been proposed for this application.[3] For mining, in situ elemental analysis technology may also be used throughout the mine site's life to continually monitor the collection of materials and to ensure that any tailings returned to the seabed are of appropriate composition to minimise impact on the surrounding ecosystem.

Ocean mining offers many benefits over land-based mining.[4] Multiple useful minerals can be recovered from a single site; there is less or no overburden; high concentrations of high quality ores are present; and mining platforms (surface vessel and associated equipment) may be easily moved to new locations. Furthermore, comparatively little infrastructure is required, and hence a smaller negative environmental footprint (e.g., roads, buildings, and open pits) may be resultant with less CO_2 produced per tonne of metal delivered. Also, ocean mining does not require displacement of indigenous peoples, and it has been reported that a less populated ecosystem would be involved compared to land-based mining[5] with the associated areas expected to be repopulated in time due to the widespread nature of the species concerned.[6]

Nevertheless, the potential environmental effects of ocean mining should not be disregarded. Likely areas to be affected include the seafloor, water column, surface, and land.[7] The removal and/or loss (smothering) of benthic organisms, due to disturbance of sediment may be significant,[8] and near surface biota may also be affected by plumes of suspended sediments.[9] As such, it is desirable to limit any negative environmental impacts so far as practicable, for example, by minimising the interaction between the collector system and seafloor; ensuring separation of minerals from sediments close to the seabed; and strip-wise mining (leaving alternate strips of undisturbed seafloor).[10] In all of these areas, in situ elemental analysis of the materials involved will be critical to achieving best results.

The minerals of interest for ocean mining are present in three forms:

1. *Polymetallic nodules* that are created via the precipitation of seawater-dissolved metallic components resulting in the formation of rock concretions (typically up to 20 cm diametre), which lay loose on the ocean abyssal planes.
2. *Cobalt-rich crusts* that are formed by the absorption of seawater metals in the rocky beds of seamount slopes.[1]
3. *Polymetallic sulphides* forming hydrothermal vent chimneys,[11] where hot (200–400 °C[12]) mineral-rich water having been heated and enriched as it was drawn through the seafloor comes into contact with cold water and thus deposits minerals around the vent, resulting in the formation of chimney-like structures called black and white smokers. Black smokers originate from the precipitation of Fe, Cu, Zn, and Pb sulphides at temperatures up to 400 °C,[13] whereas white smokers originate from the precipitation of silica and Ba or Ca sulphates from alkaline solutions at temperatures up to 300 °C.[13]

In this article, early laboratory prototype development of a GaAs X-ray detector and preamplifier electronics for a future XRF spectrometer for in situ characterisation of deep seabed minerals is reported with a specific focus on the electronics and detector physics of the detector-preamplifier system. The detector, a custom made 200 μm-diametre GaAs p^+-i-n^+ mesa photodiode with a 10 μm i layer thickness, was connected to a custom made low noise single channel charge sensitive preamplifier. The photodiode was electrically characterised in a laboratory environment at 4 °C (the ambient seawater temperature in the deep ocean) and 33 °C (the ambient temperature in proximity to the laboratory Mo target X-ray tube utilised for later measurements). Detailed noise analysis of the detector-preamplifier system was performed at both temperatures using an ^{55}Fe radioisotope X-ray source (Mn Kα = 5.9 keV; Mn Kβ = 6.49 keV). Following this, multienergy calibration of the system was performed over the energy range 4.95 to 21.17 keV at 33 °C, using known fluorescence calibration samples, thus the charge output linearity of the system determined. The response of the detector-preamplifier system to varying X-ray fluence at photon energies of 8.63 and 16.6 keV is also reported. Finally, two samples of deep seabed minerals, a manganese nodule, from the Clarion-Clipperton Fracture Zone, Pacific Ocean, and a sample of black smoker hydrothermal vent, from Rodriquez Triple Junction, Indian Ocean, were analysed using the prototype detector-preamplifier system in the laboratory environment at a temperature of 33 °C, and the expected changes in the spectra in seawater at temperature of 4 °C were investigated.

2 | INSTRUMENT DESIGN CONSIDERATIONS

To identify the elements of interest for ocean mining, it is desirable for the XRF spectrometer to be able to detect characteristic fluorescence X-rays of energy ≈1 to ≈20 keV, thus including Mg Kα (1.25 keV) through to Mo Kβ (19.6 keV),[14] with a sufficiently good energy resolution to be able to deconvolve the detected X-ray peaks from each other during processing. High intrinsic quantum detection efficiency across the energy range is also desirable because it minimises the required spectrum accumulation time. The required range of elements to be excited determines in part the choice of the X-ray excitation source. It is anticipated that dual ^{55}Fe and ^{109}Cd radioisotope X-ray sources will be used in an eventual in situ deep-sea X-ray fluorescence spectrometer similarly to the Beagle 2 XRS.[15]

Temperature tolerance is also required if work is to take place in close proximity to hydrothermal vents.

Significant work has been conducted to produce compact, low power, and temperature tolerant photon counting wide bandgap X-ray spectrometers for space science, and much of the work can be transferred to geological oceanography. At high temperatures, X-ray spectrometers benefit from wide bandgap semiconductor detectors (e.g., made from GaAs,[16,17] SiC,[18,19] AlGaAs,[20] and AlInP[21,22]) because detectors made from these materials have lower thermally generated leakage currents and thus less parallel white noise[23] than would be present in narrower bandgap materials such as Si and Ge[24] at elevated temperatures. The use of a wide bandgap detector is therefore also considered for in situ geological oceanography XRF and mining applications. Although the requirement for pressure tolerant instrumentation is undeniable (pressures ≈500 atm would be experienced at depths of 5 km[25]), there is extensive experience developing equipment able to operate in such environments within the relevant communities; for a review of this, the reader is referred to other works.[26–28]

In addition to the above challenges, the attenuation of X-rays in seawater should also be considered. The attenuation of X-rays is a function of the X-ray energy and the attenuation coefficient and thickness of the medium.[29] Seawater predominantly consists of H_2O with dissolved salts at a typical 3.5% concentration by weight.[30] The ions resulting from the dissolved salts do not appreciably affect the X-ray absorption in the energy range of interest.[31] Thus, for design of an in situ X-ray spectrometer of the type discussed, seawater can be simply regarded as H_2O. Figure 1 shows the attenuation of X-ray beam intensity in 0.5 mm and 1 mm lengths of H_2O as a function of X-ray photon energy. For comparison purposes, attenuation of X-rays through 9 cm of air (i.e., N_2 and O_2 in the appropriate ratio, for simplicity) is also shown in Figure 1. For both materials, the attenuation coefficients were extracted from Henke, Gullikson, and Davis [32]. The importance of close proximity of the X-ray spectrometer to the sample is evident from Figure 1. As an example, the intensity of 3.1 and 3.9 keV X-ray photons falls to 0.01% in 0.5 mm and 1 mm of H_2O, respectively.

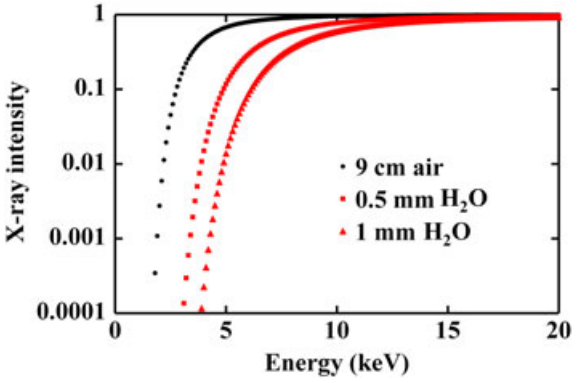

FIGURE 1 Attenuation of X-rays in 9 cm of air (black circles), and 0.5 mm (red squares) and 1 mm (red triangles) of water

Attenuation of X-rays within materials between the X-ray sources and the deep seabed minerals, as well as between the deep seabed minerals and the detector, in addition to seawater may also occur. Such layers can be the window of the radioactive exciting sources, materials (e.g., loose sediments) covering the minerals of interest, as well as the X-ray window of the detector itself. The X-ray sources and detector windows should be designed to minimise the X-ray attenuation. Additionally, the potential reduction of the count rate due to the possible presence of materials covering the deep seabed minerals should also be considered, and the possible requirement for a sample preparation tool is contemplated.

3 | EXTRA-TERRESTRIAL APPLICATIONS

In addition to the characterisation of deep seabed minerals formed by hydrothermal vents on Earth with in situ XRF analysis, there is interest in using similar instrumentation for the exploration of the oceans of icy moons, such as Europa, one of Jupiter's Galilean moons.

Images of Europa captured by the Galileo spacecraft[33] showed a surface of ice with numerous features,[34–36] and magnetometer measurements indicated the existence of an ocean under Europa's ice sheet believed to be formed from Europa's internal heating due to Jupiter's tidal pull.[37] The tidal forces generated by Jupiter could also result in the formation of a network of hydrothermal vents on Europa's ocean floor.[38] Furthermore, recent observations provided strong evidence of the existence of water plumes venting from Europa,[39,40] with a potential implication that the Europa's surface and ocean may be linked. Prototype submarine designs for future icy moon ocean exploration have already been reported.[37,41] Employing an XRF spectrometer in such a submarine for in situ characterisation would eliminate the need to return collected samples back to the surface of Europa or bring them inside the submarine. The requirement of radiation hard electronics that can survive the intense radiation environment of Jupiter also favours GaAs photodiodes; researchers have demonstrated a high radiation resistance of GaAs detectors to γ-rays,[42,43] fast neutrons,[44] and high energy electrons.[45]

4 | DETECTOR STRUCTURE

For the detector, a GaAs p^+-i-n^+ layer structure was grown to the Author's specifications at the Engineering

and Physical Sciences Research Council (EPSRC) National Centre for III-V Technologies, Sheffield, UK, on a commercial GaAs n^+ substrate by metalorganic vapour phase epitaxy. The p^+ layer, the unintentionally doped i layer, and the n^+ layer had thicknesses of 0.5 μm, 10 μm, and 1 μm, respectively. The doping concentration of both the p^+ and n^+ layers was of 2×10^{18} cm^{-3}. Mesa diodes with diameters of 200 μm were chemically etched from the wafer using 1:1:1 H_3PO_4:H_2O_2:H_2O solution followed by 10 s in 1:8:80 H_2SO_4:H_2O_2:H_2O solution. An Ohmic contact, covering 45% of the surface of the device and consisting of 20 nm of Ti and 200 nm of Au was deposited on top face of each of the detectors. A rear Ohmic contact consisting of 20 nm of InGe and 200 nm of Au was deposited on the rear of the substrate. The GaAs devices were unpassivated. A total of 14 devices with 200 μm diameters were initially electrical characterised at room temperature,[46] and a representative device was selected for use in the detector-preamplifier system presently reported.

5 | DETECTOR ELECTRICAL CHARACTERISATION

The electrical characteristics, namely the current and capacitance characteristics, of a photodiode X-ray detector in part determine the energy resolution of the detector-preamplifier system.[23] Also, measurements of the electrical characteristics of a photodiode at different bias conditions and temperatures enable the extraction of key parameters of the photodiode[47] allowing comparisons between available devices and advances to be made in understanding the physics of such devices.

The dark current of the photodiode as a function of both forward applied bias from 0 to 1 V and reverse applied bias from 0 to −50 V was measured using a Keithley 6487 Picoammeter/Voltage Source. The photodiode was installed inside a TAS Micro MT climatic cabinet for temperature control. Temperatures of 4 °C—the ambient water temperature in the deep ocean and 33 °C—the temperature at which the energy-charge (Section 7) and count rate-X-ray intensity (Section 8) linearity responses were characterised, and XRF spectra of representative geological samples were accumulated in the laboratory (Section 9). Figure 2 shows the measured currents of the photodiode at both temperatures.

The saturation current and the ideality factor of the photodiode were extracted on the basis of the linear region of the semi-logarithm dark current as a function of forward bias.[17] The saturation current was found to increase with increased temperature, as expected, from 0.046 pA ± 0.007 pA at 4 °C to 0.72 pA ± 0.06 pA at 33 °C. The ideality factor was found to be improved at 4 °C (= 1.84 ± 0.02) compared with 33 °C (= 1.96 ± 0.01), in contrast with previously reported thinner (7 μm i layer) GaAs p^+-i-n^+ X-ray photodiodes, whose ideality factor worsened at 0 °C compared with 120 °C.[17] The ideality factor of a semiconductor p^+-i-n^+ diode with low intrinsic carrier concentration, n_i, such as a GaAs diode, is expected to be close to 2 at room temperature due to the generation current dominating over the diffusion current.[47] At sufficient high temperatures, the diffusion current may dominate over the generation current, and hence, the ideality factor is expected to be improved (closer to 1). However, the forward current measurements of the reported device showed that, at both the investigated temperatures, the generation current was more dominant than the diffusion current and that the cause of the generation current was more prominent at 33 °C than at 4 °C. The deterioration of the ideality factor at 33 °C was attributed to more thermally stimulated crystal lattice defects compared to 4 °C, being the main cause of the non-ideal behaviour of the device. Defects in the crystal lattice, such as vacancies and interstitials disturbing the periodicity of the electric field in the crystal that could potentially induce charge carrier scattering, as well as dislocations and impurities with energy levels deep in the

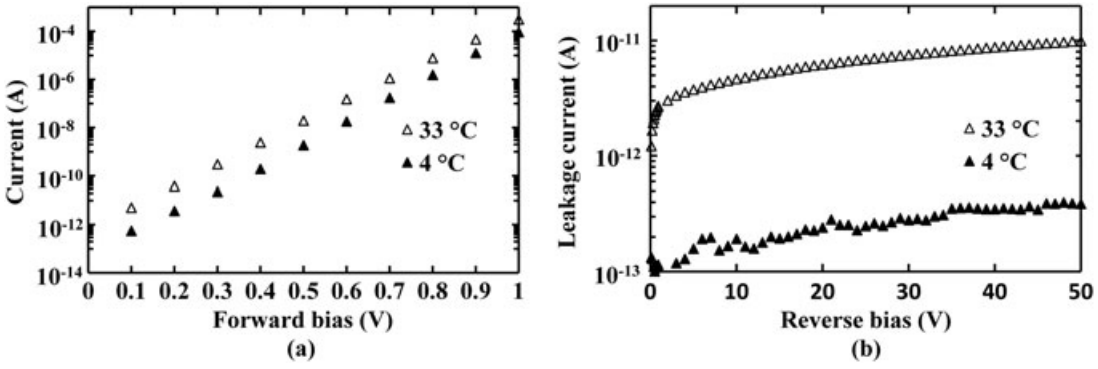

FIGURE 2 Dark current at 33 °C (empty triangles) and 4°C (filled triangles) as functions of applied (a) forward and (b) reverse bias

energy gap that could potentially act as traps or recombination centres, tend to accumulate with increased temperature and could lead to non-ideal behaviours.

The leakage current of the device was found to increase with increased temperature from 0.4 pA (1.2 nA/cm^2) at 4 °C to 9.9 pA (31.6 nA/cm^2) at 33 °C, both at the highest investigated reverse bias, −50 V (~50 kV/cm internal electric field). The reported photodiode had comparable leakage current density with other high quality GaAs p^+-i-n^+ X-ray photodiodes; as an example, a leakage current density of 23 nA/cm^2 at 33 °C was measured for the currently reported photodiode compared to 92 nA/cm^2 at 30 °C for another high quality device[48] both at internal electric field strengths of ~30 kV/cm. The stability of the leakage current with time was investigated. The photodiode was kept reverse biased at −15 V, and its leakage current was measured over a period of 8 hr, every 1 min, at 33 °C. The leakage current time stability of the photodiode at −15 V reverse bias and 33 °C can be seen in Figure 3 along with the calculated white parallel noise contribution at 1 μs, as described in Section 6.

The leakage current increased from 5.8 (corresponding to 8 e^- rms) to 15 pA (corresponding to 13 e^- rms) after 2.5 hr and remained stable thereinafter. The source of leakage current time instability is related to the mechanism of conduction.[49] As an example, the slow decrease of the leakage current with time has been previously attributed to the generation current being stable after some time of the application of the bias, whereas leakage current increase with time has been previously related to peripheral leakage current due to possible charge build-up in the passivation layer.[49] The slow and logarithmic increase of leakage current of the currently reported GaAs p^+-i-n^+ photodiode at 33 °C and −15 V reverse bias over the first 2.5 hr is currently unknown, but it may be attributed to the presence of crystal defects acting as traps or recombination centres affecting the leakage current. The relatively low (0.4 pA at 4 °C and 9.9 pA at 33 °C, both at ~50 kV/cm internal electric field) and stable leakage current density of the GaAs detector is advantageous for minimising the white parallel noise of the reported prototype detector-preamplifier system.

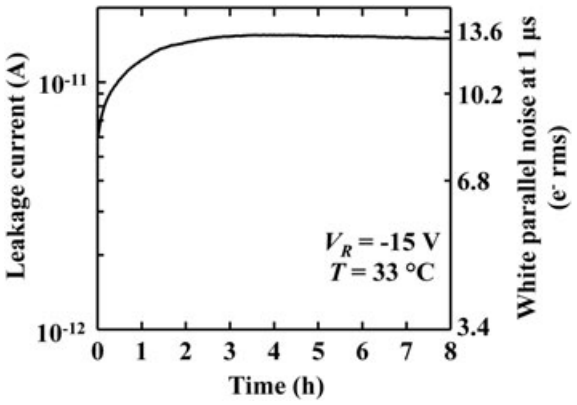

FIGURE 3 Dark current measured at −15 V reverse bias and 33 °C as a function of time. The right x-axis shows the corresponding white parallel noise contribution of the measured dark current at 1 μs shaping time

The depletion layer width and the effective doping concentration of the i layer, as well as the white series noise contribution (see Section 6) of the photodiode were all determined from capacitance measurements. The capacitance measurements were performed using an HP 4275A Multi Frequency LCR metre with 50 mV rms magnitude and 1 MHz frequency test signal. Figure 4 shows the measured junction capacitance as a function of forward and reverse bias at 4 and 33 °C. The capacitance of the package (0.76 pF at 4 °C and 0.95 pF at 33 °C) was subtracted from the total measured capacitance to give the junction capacitance shown in Figure 4. The total uncertainty in the capacitance measurements, including the uncertainty in the LCR metre, packaging capacitance, and the root mean square error, was estimated to be ±0.03 pF.

The forward biased junction capacitance at 1 V was measured to increase with increased temperature, from 2.58 pF at 4 °C to 3.27 pF at 33 °C. There was a significant contribution of the diffusion capacitance to the junction capacitance at forward applied biases due to the rearrangement of the minority carrier density.[47] The increase in the forward biased junction capacitance with increased temperature was attributed to the higher forward current at 33 °C compared to that at 4 °C (Figure 2a), because the diffusion capacitance is directly proportional to the forward current.

The depletion layer capacitance, defining the junction capacitance at applied reverse biases, was found to be temperature invariant for reverse biases (magnitude) >−3 V, at the investigated temperatures within the measurement error. It was measured to be 0.38 pF at −50 V reverse bias both at 4 °C and 33 °C. The low capacitance of the GaAs detector is beneficial for minimising the white series noise of the reported prototype detector-preamplifier system. However, a temperature dependent depletion layer capacitance was measured for applied reverse biases ranging from 0 to −3 V. The depletion layer width of the photodiode was calculated using the measured depletion layer capacitance[17] as a function of applied reverse bias for both temperatures and can be seen in Figure 5.

The depletion layer width of the photodiode was determined to only slightly increase with increased reverse bias; it was found to increase from 9.2 ± 0.7 μm at 0 V to 9.8 ± 0.8 μm at −50 V reverse bias and 4 °C

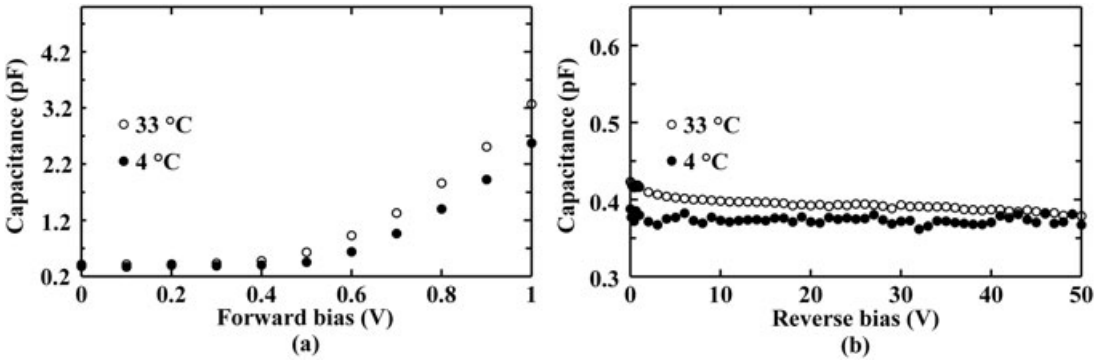

FIGURE 4 Capacitance as a function of (a) forward and (b) reverse bias measured at 33 °C (empty circles) and 4 °C (filled circles)

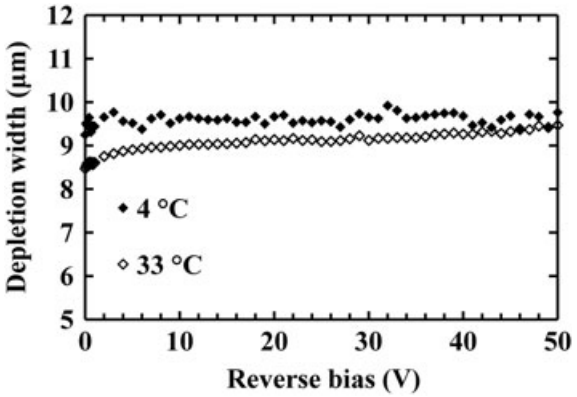

FIGURE 5 Calculated depletion layer width at 4 °C (filled diamonds) and 33 °C (empty diamonds), calculated from capacitance measurements as a function of applied reverse bias

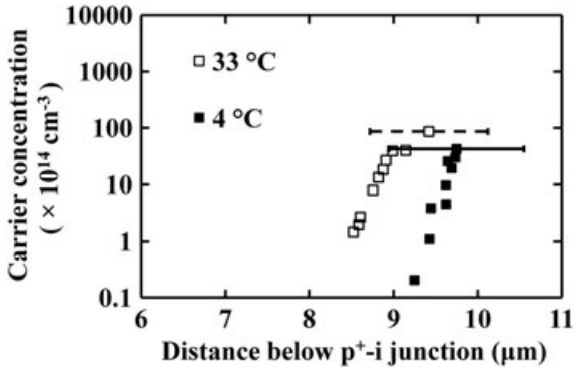

FIGURE 6 Calculated effective doping concentration as a function of distance below p^+-i junction at 4 °C (filled squares) and 33 °C (empty squares) determined from capacitance measurements. The uncertainty of the i layer thickness (greatest depletion layer width) at 4 °C and 33 °C, as calculated by propagating the uncertainty in the capacitance measurement (±0.03 pF), can also be seen

and from 8.5 ± 0.5 μm at 0 V to 9.5 ± 0.7 μm at −50 V reverse bias and 33 °C. Another observation based on Figure 5 is that the photodiode was almost fully depleted at −1 V reverse bias, when operating at 4 °C whereas the same occurred at a higher reverse bias, when operating at 33 °C. This might be explained by the presence of a thin region around the depletion region with non-ionised dopants at 4 °C that were ionised at 33 °C and limited the extension of the depletion layer at low reverse biases.[50]

The majority carrier concentration, approximated to the effective i layer doping concentration as a function of distance below the p^+-i junction, was calculated using the differential capacitance method[17] and is shown in Figure 6. It was found to increase from 0.2×10^{14} cm^{-3} at 9.2 ± 0.7 μm below the p^+-i junction to 43×10^{14} cm^{-3} at the i-n^+ interface, at 4 °C. Similarly, the effective doping density was found to increase from 1×10^{14} cm^{-3} at 8.5 ± 0.5 μm below the p^+-i junction to 86×10^{14} cm^{-3} at the i-n^+ interface, at 33 °C. The uncertainties of the depletion layer widths were calculated propagating the uncertainty in the capacitance measurements (± 0.03 pF). However, it should be noted that the doping profile of the i layer (Figure 6) determined using the differential capacitance method had a spatial resolution of the order of one Debye length, which has been calculated to be 0.4 μm for GaAs with a doping concentration of 10^{14} cm^{-3} in the temperature range 4 °C to 33 °C.[47]

6 | MEASUREMENTS WITH AN ^{55}FE RADIOISOTOPE X-RAY SOURCE

The performance of the detector-preamplifier system was initially characterised with ^{55}Fe X-ray measurements at 4 °C. In this section, the different noise contributions of the system at 4 °C are discussed. The relative performance of the system at 33 °C, which is the temperature of the subsequent measurements using the Mo target X-ray tube, is also shown.

The GaAs p^+-i-n^+ photodiode was connected to the input of a custom made, single channel charge sensitive preamplifier. The preamplifier was of feedback resistorless design, similar to Bertuccio,Rehak, and Xi[51], having a Vishay Siliconix 2N4416A junction field-effect transistor (JFET) for the input transistor.[52] An ^{55}Fe radioisotope

X-ray source was positioned 3 mm above the top of the device. The detector along with the preamplifier were installed inside a TAS Micro MT climatic cabinet throughout the measurements for temperature control. The signal of the preamplifier was shaped using an Ortec 572A shaping amplifier and was further connected to a multichannel analyser for digitisation. The live time limit for each accumulated spectrum was 60 s.

The temperature was initially set to 4 °C; the detector was kept reverse biased at −15 V, and spectra were accumulated for shaping times, τ, =0.5, 1, 2, 3, 6, and 10 μs. Then, the temperature was increased to 33 °C, and ^{55}Fe X-ray spectra were obtained for the same shaping times. The accumulated spectra of the ^{55}Fe radioisotope X-ray source at 4 °C and 33 °C with the best energy resolution (lowest full width at half maximum, *FWHM*) can be seen in Figure 7. The detected ^{55}Fe photopeak was the combination of the characteristic Mn Kα (5.9 keV) and Mn Kβ at (6.49 keV) lines of the ^{55}Fe radioisotope X-ray source.[53] Gaussians were fitted to the peak taking into account the relative emission ratio[53] and the relative efficiency of the detector for the 5.9 and 6.49 keV peaks. The spectra were energy calibrated based on the positions of the zero energy noise peak and the Mn Kα peak. The uncertainty of the *FWHM* associated with fitting a Gaussian to the photopeak was estimated to be ±10 eV. The energy resolution degraded from 580 eV at 4 °C to 680 eV at 33 °C, both at −15 V reverse bias and 2 μs shaping time. The difference in the peak height between the spectrum obtained at 4 °C (1,146 counts at the centroid channel of the 5.9 keV peak) and the spectrum obtained at 33 °C (960 counts at the centroid channel of the 5.9 keV peak) was attributed to the difference in the *FWHM* between these two spectra: the total counts (over 60 s accumulation time) within the energy range 2 and 8 keV was 89,680 and 89,335 for the spectrum accumulated at 4 °C and 33 °C, respectively. The *FWHM* was measured for all obtained spectra and can be seen in Figure 8 as a function of shaping time. The optimum shaping time was found to be 2 μs for both temperatures.

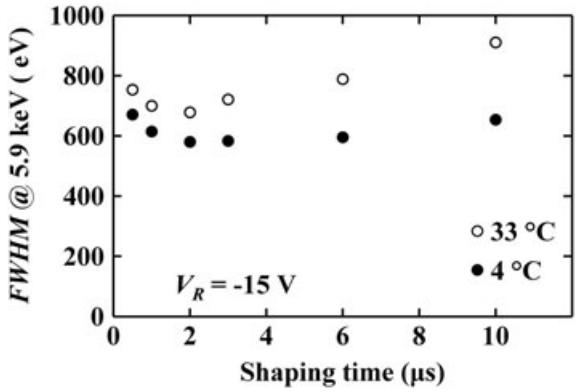

FIGURE 8 Full width at half maximum (*FWHM*) at 5.9 keV at 4 °C (filled circles) and 33 °C (empty circles) as a function of shaping time at −15 V reverse bias

For a detector-preamplifier system consisting of a non-avalanche semiconductor detector coupled to a charge sensitive preamplifier, assuming the incomplete charge collection noise is negligible; its energy resolution is degraded due to two independent sources of noise: Fano noise and electronic noise.[54] The Fano noise was calculated to be 128 eV at 5.9 keV assuming an electron hole pair creation energy of 4.184 eV[55] and a Fano factor of 0.12.[56] The electronic noise, due to the detector itself and the preamplifier comprises white parallel noise, white series noise (including the induced gate current noise contribution), 1/f noise, and dielectric noise.[23] The white parallel noise, due to the leakage current of the detector and of the input JFET of the preamplifier, is directly proportional to the shaping time. The white series noise, due to the capacitance of the detector and of the input JFET, is inversely proportional to the shaping time, τ. The 1/f and dielectric noise are both shaping time invariant. Hence, the experimental values of *FWHM* as a function of shaping time can be fitted through a multidimensional least squares estimation method to find the three parameters each of which has a different relationship with τ.[57]

A multidimensional unconstrained nonlinear minimisation was applied to the *FWHM* as a function of

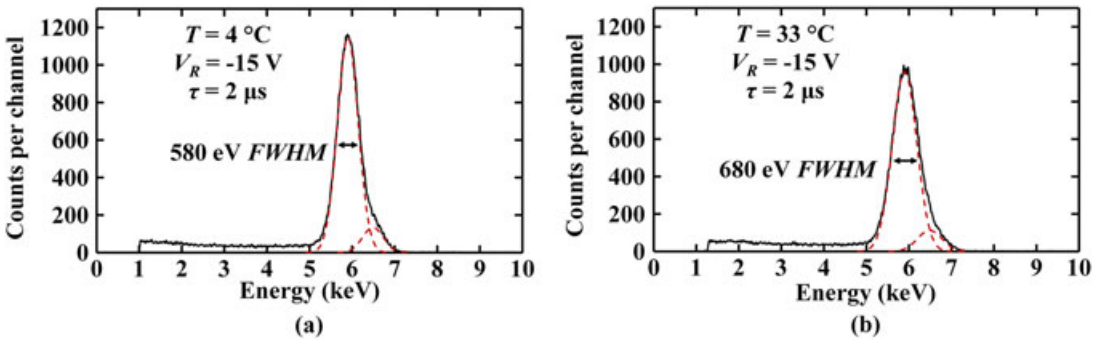

FIGURE 7 ^{55}Fe spectra at (a) 4 °C and (b) 33 °C accumulated with the detector-preamplifier system (GaAs photodiode detector reverse biased at −15 V) at 2 μs shaping time, along with the fitted Mn Kα and Kβ peaks (dashed lines). *FWHM* = full width at half maximum

shaping time (Figure 8) for both temperatures and the fitting can be seen in Figure 9.

The equivalent total capacitance and leakage current of the system were estimated from the $1/\tau$ and τ proportional contributions, respectively. A total input capacitance,

$$C_T = C_D + C_i + C_f + C_s, \quad (1)$$

where C_D is the detector capacitance; C_i is the input JFET capacitance; C_f is the feedback capacitance, and C_s is the stray capacitance[23] of 3.90 pF, and 4.12 pF was estimated for the detector-preamplifier system when operated at 4 °C and 33 °C, respectively. This capacitance was attributed to the capacitance C_D of the packaged detector at −15 V reverse bias, which was measured to be 1.13 and 1.35 pF at 4 °C and 33 °C, respectively, to the capacitance C_i of the input JFET of the preamplifier (2 pF[52]), to the feedback capacitance C_f of the preamplifier, and to the stray capacitance, C_s. A total leakage current,

$$I_L = 2(I_{LD} + I_{DG}), \quad (2)$$

where I_{LD} is the detector leakage current, and I_{DG} is the input JFET drain to gate leakage current[23] of 13.35 pA, and 44.07 pA was estimated for 4 °C and 33 °C, respectively. Hence, the measured *FWHM* as a function of shaping time suggests that the sum of detector and input JFET leakage current was 6.67 and 22.03 pA at 4 °C and 33 °C, respectively. The input JFET drain to gate leakage current was regarded negligible (<1 pA) at the investigated temperatures, and thus the contributed leakage current was attributed to the detector being reverse biased at −15 V.

The shaping time invariant noise contribution, consisting the Fano, 1/*f*, and dielectric noise was estimated to be 512 and 565 eV at 4 °C and 33 °C, respectively. Subtracting in quadrature the calculated Fano noise at 5.9 keV and 1/*f* noise[23] from the total shaping time invariant noise contribution, the dielectric noise of the system can be calculated. It was found to be 495 eV (corresponding to 50 e^- rms equivalent noise charge contribution) and 550 eV (corresponding to 56 e^- rms equivalent noise charge contribution) at 4 °C and 33 °C, respectively. The dielectric noise, attributed to lossy dielectrics at the input of the preamplifier, such as those of the feedback capacitance, the passivation of the input JFET surface, the detector and input JFET themselves, and the packaging of the detector and input JFET, was found to be the dominant source of noise at all investigated shaping times and both temperatures, at −15 V reverse bias except at long shaping times at 33°C. At shaping times >6 μs (as deduced from Figure 9b), the leakage current of the detector being reverse biased at −15 V and operating at 33 °C was found to give rise to the most significant noise contribution, the parallel white noise. The increase of the dielectric noise at 33 °C compared to 4 °C is in accordance with the expected change in dielectric noise considering its relationship with the temperature and the capacitance.[23] Overall, the degradation of the energy resolution at 33 °C compared to 4 °C was attributed to both the leakage current and dielectric noise increase.

7 | ENERGY CALIBRATION OF THE DETECTOR-PREAMPLIFIER SYSTEM

The GaAs p^+-i-n^+ photodiode was connected to the input of the same custom made, single channel charge sensitive preamplifier used for the obtained spectra of an ^{55}Fe radioisotope X-ray source (Section 6). The photodiode and preamplifier were installed in a custom housing that had a 4 μm-thick Al foil X-ray window. The housing was installed within an LD Didactic GmbH X-ray apparatus (part number 554 801) with a Mo target X-ray tube. A custom made Al collimator lined with

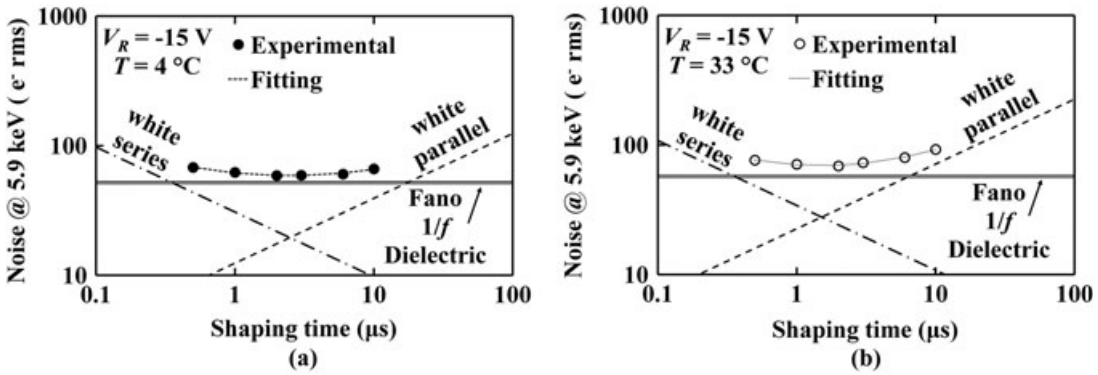

FIGURE 9 Equivalent noise charge at (a) 4 °C and (b) 33 °C as a function of shaping time. The three noise contributions, inversely proportional to shaping time (white series), directly proportional to shaping time (white parallel), and shaping time invariant (Fano, 1/*f*, and dielectric) have been determined with a multidimensional unconstrained nonlinear minimisation of the experimental points

polytetrafluoroethylene (PTFE) (to absorb all fluorescence from the Al) was used to collimate the X-rays from the Mo target X-ray tube. The preamplifier and the photodiode were attached to the goniometer of the apparatus for precise positioning. The output of the preamplifier was connected to an Ortec 572A shaping amplifier. The output of the shaping amplifier was then connected to an Ortec EASYMCA multichannel analyser for digitisation.

Characterisation of the energy-charge response linearity of the detector-amplifier system was performed using nine high purity metal XRF calibration targets of known composition (Table 1).

A diagram of the experimental set up can be seen in Figure 10. It should be noted here that the set up shown in Figure 10 does not represent the final XRF spectrometer geometry. The calibration foils and the detector-preamplifier system were positioned at 45° and 135° to the collimator, respectively. This arrangement minimised the detection of photons directly from the X-ray tube and the detection of scattered X-rays from the tube, although maximising the detection of fluorescence X-rays from the calibration foils. The distance between the foils and the detector was 9 cm (air). X-ray spectra of each foil were accumulated, each spectrum had a live time limit of 3 hr. The X-ray tube voltage and current was set to 35 kV and 1 mA, respectively. The X-ray tube was powered for 3 hr prior to any measurements in order for the temperature of the system to stabilise at 33 °C (measured at the detector). The detector was reverse biased at −15 V throughout the measurements and the shaping time of the shaping amplifier was set to 1 μs.

TABLE 1 Fluorescence samples used in this work with the corresponding primary X-ray emission line energies used for calibration[14]

Material (primary line)	Line energy (keV)
V (Kα)	4.95
Cr (Kα)	5.41
Mn (Kα)	5.89
Cu (Kα)	8.04
Zn (Kα)	8.63
Au (Lα)	9.71
Ge (Kα)	9.88
Au (Lβ)	11.44
Nb (Kα)	16.61
Pd (Kα)	21.17

Gaussians were fitted to the peaks of each accumulated spectra. The centroid channel number of each fitted peak from each fluorescence calibration sample along with the accepted energies of those peaks were used to energy calibrate the system. The plot of the multichannel analyser channel number as a function of energy can be seen in Figure 11. The voltage output of the detector-preamplifier system had a linear relationship with photon energy, and the line of best fit was calculated using linear least squares fitting.

The energy resolution (*FWHM*) of each fitted photopeak was measured and can be seen in Figure 12. It was found to increase from 695 eV at 4.95 keV to 735 eV at 21.17 keV. The *FWHM* was attributed to the Fano noise[58] and to the electronic noise, because it was found that the contribution of the incomplete charge collection noise was insignificant for the detector employed in the reported detector-preamplifier system, even at −5 V reverse bias.[46] Electronic noise was expected to be energy invariant[23] (see Section 6). However, the Fano noise was expected to increase with increasing photon energy, as per

$$\Delta E[\mathrm{eV}] = 2.355\omega\sqrt{\frac{FE}{\omega}}, \tag{3}$$

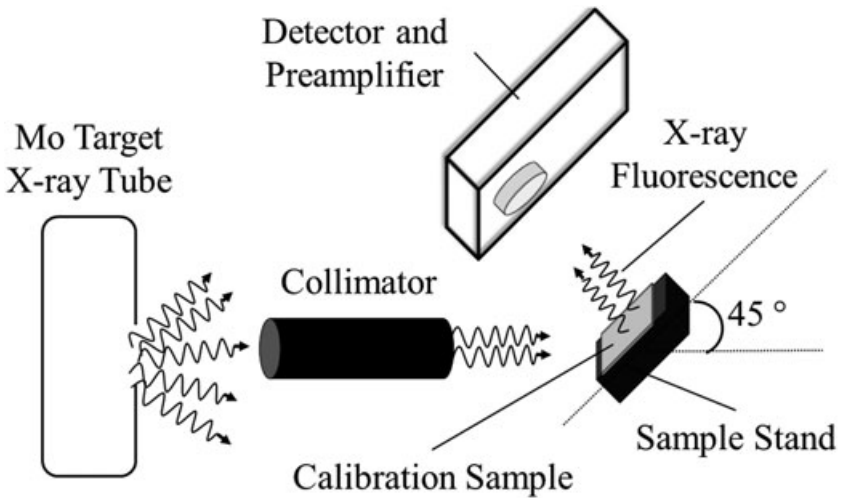

FIGURE 10 Diagram showing the experimental set up of the energy response linearity characterisation of the detector-preamplifier system

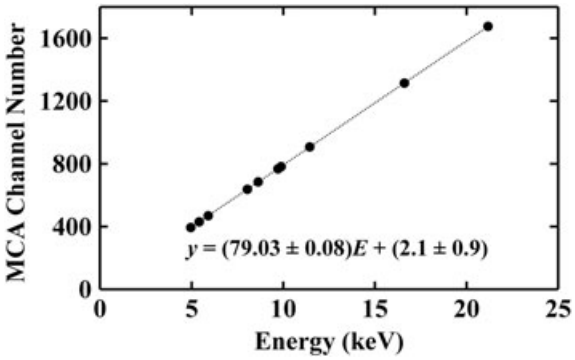

FIGURE 11 Centroid multichannel analyser (MCA) channel number for the GaAs detector-preamplifier system as a function of energy of the incoming X-ray fluorescence photons. The line of best fit, as calculated using linear least squares fitting, can also be seen

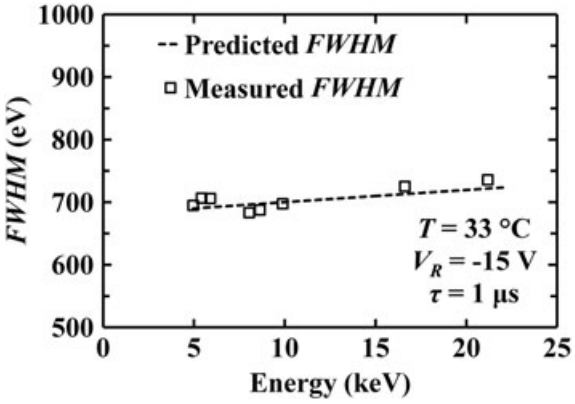

FIGURE 12 Full width at half maximum (*FWHM*) across the measured energy range. The Au Lα and Lβ peaks were excluded from this graph due to difficulty of deconvolving them

where ΔE is the *FWHM* due to Fano noise; ω is the electron-hole pair creation energy, and F is the Fano factor.[58] The Fano noise was calculated to increase from 117 eV at 4.95 keV to 242 eV at 21.17 keV, assuming an electron-hole pair creation energy of 4.184 eV[55] and a Fano factor of 0.12.[56] The electronic noise was calculated by subtracting in quadrature the Fano noise at each energy from the total measured *FWHM*. It was found to be energy invariant with a mean of 680 ± 30 eV. Its root mean square (rms) deviance was attributed to the error in fitting the photopeaks (±10 eV) and to possible small leakage current instabilities of the detector throughout the measurements resulting in variations of the white parallel noise contribution (see Section 6). The predicted *FWHM* can also be seen in Figure 12. It was calculated assuming that the total *FWHM* comprised the electronic noise (=680 eV) and the Fano noise calculated at each energy, and it was in good agreement with the measured *FWHM*.

8 | DETECTOR-PREAMPLIFIER SYSTEM LINEARITY WITH X-RAY INTENSITY

In the previous section, for the energy calibration of the system, the X-ray flux was kept at its maximum by setting the X-ray tube current, X_c, to 1 mA. In this section, the response of the system with varied X-ray intensity was investigated using two of the fluorescence calibration foils, Zn (Kα = 8.63 keV) and Nb (Kα = 16.6 keV). This was achieved by measuring the detected count rate (counts per second), R, in the Kα peak of the two foils as a function of X-ray tube current. The same spectrum accumulation procedure was followed as for the energy calibration of the system. Spectra were accumulated with the X-ray tube current, X_c, at 0.2 to 1 mA, in 0.2 mA steps. The count rate (counts per second contributing to each Kα peak), at both 8.63 and 16.6 keV, was determined as a function of X-ray tube current and can be seen in Figure 13.

A linear relationship was found for the detector-preamplifier system with varying X-ray tube current. The line of best fit was calculated using linear least squares fitting and can be seen in Figure 13. The linearity between the count rate of the system and the XRF photons entering the detector is an important characteristic of the XRF spectrometer for quantitative XRF analysis.

9 | ELEMENTAL ANALYSIS OF DEEP SEABED MINERALS

X-ray fluorescence spectra of a manganese nodule, from the Clarion-Clipperton Fracture Zone, Pacific Ocean, and a sample of black smoker hydrothermal vent, from Rodriquez Triple Junction, Indian Ocean, were

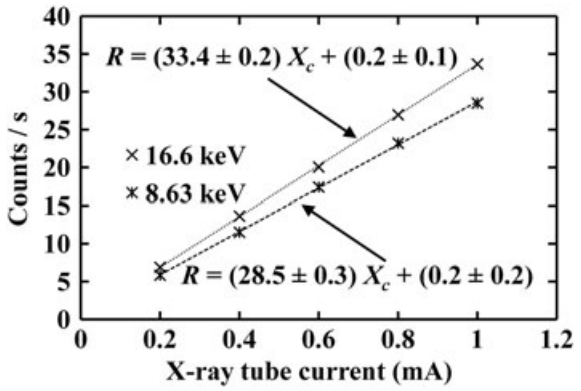

FIGURE 13 Detected count rate (counts per second), R, in the Zn Kα peak (=8.63 keV) and Nb Kα peak (=16.6 keV) as a function of X ray tube current, X_c, using the present GaAs detector-preamplifier system. The lines of best fit calculated using linear least squares fitting can also be seen

accumulated using the GaAs detector-preamplifier system. The procedure followed for obtaining spectra of the samples was the same as that used for the calibration foils. The detector was reverse biased at −15 V throughout the measurements, and the shaping time of the shaping amplifier was set to 1 μs. Each spectrum was accumulated for 8 hr. A background spectrum (without each geological sample) was also accumulated for the same period of time and subtracted from the obtained spectra. The resulting spectra for the manganese nodule and the black smoker can be seen in Figure 14 and Figure 15, respectively.

For each spectrum, the centroid energies of the main photopeaks were found, and the elements of the deep seabed minerals were identified. This was achieved with the aid of the energy calibration equation found for this system. The elements present in each sample were identified by the energies of their X-ray emission lines.[14]

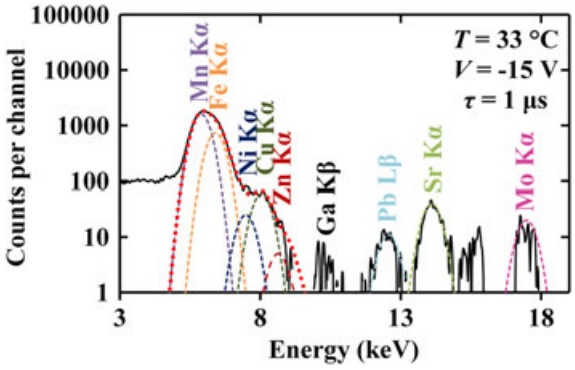

FIGURE 14 Accumulated X-ray fluorescence spectrum of a manganese nodule using the GaAs detector-preamplifier system. The fitted Mn Kα (purple), Fe Kα (orange), Ni Kα (blue), Cu Kα (green), Zn Kα (dark red), Pb Lβ (light blue), Sr Kα (light green), and Mo Kα (magenta) can be seen. The red dotted line corresponds to the sum of Mn, Fe, Ni, Cu, and Zn Kα and Kβ peaks

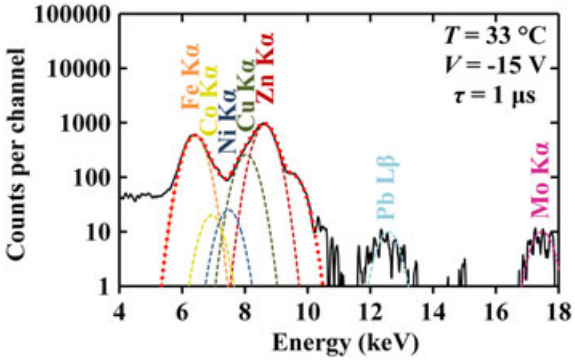

FIGURE 15 Accumulated X-ray fluorescence spectrum of a black smoker using the GaAs detector-preamplifier system. The fitted Fe Kα (orange), Co Kα (yellow), Ni Kα (blue), Cu Kα (green), Zn Kα (dark red), Pb Lβ (light blue), and Mo Kα (magenta) can be seen. The red dotted line corresponds to the sum of Fe, Co, Ni, Cu, and Zn Kα and Kβ peaks

The predicted *FWHM* defined previously was used to fit the main photopeaks of each spectrum. A multipeak fit, for peaks not being able to be resolved, was achieved by fitting the heights of the emission lines of the potential elements using the energies of their X-ray emission lines,[14] the predicted *FWHM* of the system at each energy and the relative emission ratio[59] and the relative efficiency of the detector for their Kα and the Kβ peaks.

The major and trace elements found in the manganese nodule were Mn, Fe, Ni, Cu, Zn, Pb, Sr, and Mo (Figure 14). This is in agreement with the elements found in previously reported elemental analysis of polymetallic nodules from the Central Indian Basin.[60] Also, manganese nodules from the Clarion-Clipperton Fracture Zone region were previously found to consist of Mn, Fe, Ni, Cu, Zn, Pb, and Mo.[61] Although such nodules were also found to consist of Co (Kα at 6.9 keV[14]) at an average composition of 0.23%, such a finding cannot be deduced for the presently reported manganese nodule.

The major elements identified in the black smoker were Fe, Co, Ni, Cu, Zn, Pb, and Mo (Figure 15). The most commonly observed minerals in previously studied black smokers were Fe, Cu, and Zn sulphides.[12] Mineralogical studies of sulphide chimneys from the Central Indian Ridge (north of the Rodriguez Triple Junction), Indian Ocean, showed a high cumulative Cu, Fe, and Zn concentrations close to 50–60 wt.%.[62] They also showed high Co, Mo, and As (Kα at 10.5 keV[14]) contents.

The accumulated XRF spectra of the manganese nodule and the black smoker in the laboratory environment were then corrected to produce the XRF spectra expected to be accumulated at 4 °C in seawater, assuming the same XRF photons emitted from the samples. The XRF spectra of Figures 14 and 15 were first adjusted for the improved *FWHM* at 4 °C compared to 33 °C. The energy resolution

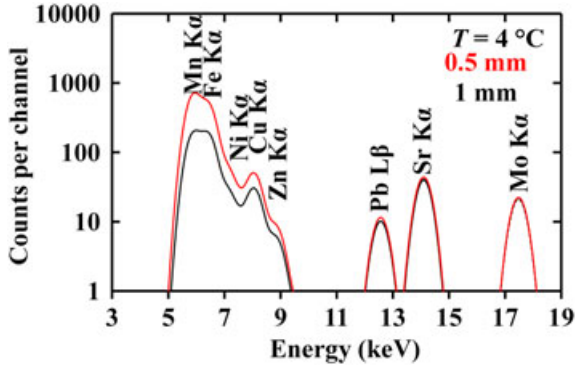

FIGURE 16 Simulated X-ray fluorescence spectrum of the manganese nodule at 4 °C in H_2O, accounting for the improved full width at half maximum and the higher attenuation of X-ray fluorescence photons in 0.5 mm (red) and 1 mm (black) H_2O. The individual peaks (Mn Kα, Fe Kα, Ni Kα, Cu Kα, and Zn Kα) comprising the multi peak have been excluded for clarity

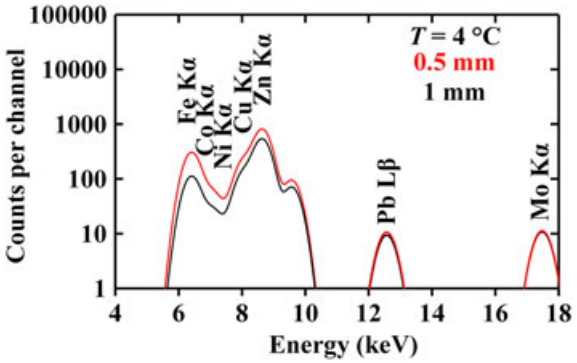

FIGURE 17 Simulated X-ray fluorescence spectrum of the black smoker sample at 4 °C in H_2O, accounting for the improved full width at half maximum and the higher attenuation of X-ray fluorescence photons in 0.5 mm (red) and 1 mm (black) H_2O, compared to the obtained X-ray fluorescence spectrum in the laboratory environment (9 cm of air). The individual peaks (Fe Kα, Co Kα, Ni Kα, Cu Kα, and Zn Kα) comprising the multi peak have been excluded for clarity

(*FWHM*) of the detector-preamplifier system at 5.9 keV was found to improve by 390 eV, from 700 eV at 33 °C (1 μs) to 580 eV at 4 °C (2 μs; see Section 6). The number of detected photons comprising each identified peak was then adjusted accordingly to account for the difference in the X-ray attenuation in air (9 cm) and H_2O (0.5 mm and 1 mm; see Figure 1). The resulted spectra can be seen in Figure 16 (manganese nodule) and Figure 17 (black smoker). Although the difference in the X-ray attenuation between 0.5 mm and 1 mm of H_2O at higher energies (≥10 keV) can be regarded negligible, this was not the case for the low energy range (<10 keV). Figures 16 and 17 emphasise the importance of close proximity (e.g., 0.5 mm and 1 mm) of the XRF spectrometer to the sample for in situ measurements and are not indicative of the count rate of the final XRF spectrometer, because the primary source of radiation and geometry of the XRF spectrometer will be different compared to the laboratory set up (Figure 10) used for the accumulation of the currently reported XRF spectra.

The dielectric noise was found to be the dominant source of noise at 4 °C (see Section 6). An improved design of the preamplifier's front-end and the elimination of the packaging of both the detector and the input JFET would lead to better energy resolution compared to the currently reported detector-preamplifier system.

10 | CONCLUSION AND FUTURE WORK

A prototype X-ray detector-preamplifier system, employing a GaAs p^+-i-n^+ photodiode with a 10 μm i layer, has been subject to preliminary study for its suitability for in situ elemental analysis of deep seabed minerals using XRF. The GaAs photodiode was initially electrically characterised at 4 °C and 33 °C; the detector-preamplifier system was then characterised at the same temperatures, and the elemental analysis of the two deep seabed minerals was performed at 33 °C.

The relatively low (0.4 pA at 4 °C and 9.9 pA at 33 °C, both at ~50 kV/cm internal electric field) and stable leakage current density of the GaAs detector (comparable with other high quality GaAs p^+-i-n^+ photodiodes[48]) is advantageous for minimising the white parallel noise of the reported prototype detector-preamplifier system. The low capacitance (0.38 pF at −50 V) of the GaAs detector is beneficial for minimising the white series noise of the reported prototype detector-preamplifier system.

The detector-preamplifier system had an energy resolution (*FWHM* at 5.9 keV) of 580 eV at 4 °C and 680 eV at 33 °C. The measured *FWHM* as a function of shaping time at 4 °C suggested the presence of 3.90 pF total capacitance and 13.35 pA total leakage current at the input of the preamplifier with additionally 50 e^- rms equivalent noise charge contribution of the dielectric noise. Similarly, the measured *FWHM* as a function of shaping time at 33 °C suggested the presence of 4.12 pF total capacitance and 44.07 pA total leakage current at the input of the preamplifier with additionally 56 e^- rms equivalent noise charge contribution of the dielectric noise.

The detector-preamplifier system was then characterised over the energy range 4.95 to 21.17 keV at 33 °C, using nine known fluorescence calibration targets to energy calibrate the system; the system output had a linear relationship with photon energy. The *FWMH* of each photopeak of all calibration targets was found to increase from 695 eV at 4.95 keV to 735 eV at 21.17 keV. The electronic noise was found to be energy invariant having mean value of 680 ± 30 eV over the measured energy range. Additionally, the relationship of the system's response was investigated as a function of varied X-ray intensity using two fluorescence calibration samples, Zn (Kα at 8.63 keV) and Nb (Kα at 16.6 keV), and found to be linear.

Two different deep seabed minerals, a manganese nodule from the Pacific Ocean and a black smoker from the Indian Ocean, were analysed for their elemental composition using the same Mo target X-ray tube and the GaAs detector-preamplifier system. It was found that the manganese nodule consisted of Mn, Fe, Ni, Cu, Zn, Pb, Sr, and Mo. The black smoker was found to consist of Fe, Co, Ni, Cu, Zn, Pb, and Mo. All were in agreement with previous studies of manganese nodules[60,61] and black smokers.[12,62] The XRF spectra that would be expected to be accumulated from these samples had they been in seawater at distances of 0.5 mm and 1 mm from

the instrument at a temperature of 4 °C were simulated and emphasised the importance of close proximity of the XRF spectrometer to the sample.

An XRF spectrometer can potentially provide insight into hydrothermal processes and revolutionise seabed mining activities with in situ characterisation of the seabed minerals. Another potential application of the reported GaAs detector-preamplifier system could be for future space missions to icy moons, such as Europa, and the exploration of their oceans. Part of the future work is the exploration of the use of the spectrometer in high temperature environments (up to 200 °C) as well as improving the energy resolution of the system by further developing the preamplifier electronics.

ACKNOWLEDGEMENTS

This work was in part supported by the Science and Technology Facilities Council, United Kingdom, through grants ST/M004635/1 and ST/P001815/1 (A. M. B., P. I.). A. M. B. acknowledges funding from the Leverhulme Trust, United Kingdom, in the form of a 2016 Philip Leverhulme Prize. G. Lioliou acknowledges funding received in the form of a PhD scholarship (2014–2016) from University of Sussex, United Kingdom. Authors' Data Statement: Data underlying this work are subject to commercially confidentiality. The Authors regret that they cannot grant public requests for further access to any data produced during the study, however the key findings are fully included within the article.

ORCID


G. Lioliou http://orcid.org/0000-0002-6989-7106

REFERENCES

[1] S. W. Park, LOSI Conference on Securing the Ocean for the Next Generation, Seoul, **2012**.

[2] M. Colazingari, *Marine Natural Resources and Technological Development: An Economic Analysis of the Wealth from the Oceans*, Routledge, Oxfordshire **2008**.

[3] G. Smith, S. Leach, EP 2877840 A1, **2015**.

[4] J. R. Hein, K. Mizell, A. Koschinsky, T. A. Conrad, *Ore Geol. Rev.* **2013**, *51*, 1.

[5] B. Agarwal, P. Hu, M. Placidi, H. Santo, J. J. Zhou, LRET Collegium 2012 Series, University of Southampton, **2012**.

[6] S. D. Scott, *Geosci. Can.* **2001**, *28*, 87.

[7] R. Sharma, *Mar. Technol. Soc. J.* **2011**, *45*, 28.

[8] R. E. Boschen, A. A. Rowden, M. R. Clark, J. P. A. Gardner, *Ocean Coast. Manage.* **2013**, *84*, 54.

[9] C. L. Morgan, N. A. Odunton, A. T. Jones, *Mar. Georesour. Geotec.* **1999**, *17*, 307.

[10] R. Sharma, *Procedia Earth Planet. Sci.* **2015**, *11*, 204.

[11] B. Kohler, A. Singer, P. Stoffers, *Clays Clay Miner.* **1994**, *42*, 689.

[12] K. L. Von Damm, *Annu. Rev. Earth Planet. Sci.* **1990**, *18*, 173.

[13] M. Gargaud, R. Amils, J. C. Quintanilla, H. J. Cleaves, W. M. Irvine, D. L. Pinti, M. Viso, *Encyclopedia of Astrobiology*, Springer-Verlag, Berlin **2011**.

[14] A. Thompson, D. Attwood, E. Gullikson, M. Howells, K. J. Kim, J. Kirz, J. Kortright, I. Lindau, Y. Liu, P. Pianetta, A. Robinson, J. Scofield, J. Underwood, G. Williams, H. Winick, *X-Ray Data Booklet (Center for X-Ray Optics and Advanced Light Source)*, Lawrence Berkeley National Laboratory, Berkeley **2009**.

[15] D. L. Talboys, P. J. Potts, G. W. Fraser, G. Butcher, D. Wegrzynekc, *X ray Spectrom.* **2009**, *38*, 417.

[16] A. M. Barnett, J. E. Lees, D. J. Bassford, J. S. Ng, C. H. Tan, N. Babazadeh, R. B. Gomes, *Nucl. Instrum. Methods Phys. Res., Sect. A* **2011**, *657*, 336.

[17] G. Lioliou, X. Meng, J. S. Ng, A. M. Barnett, *J. Appl. Phys.* **2016**, *119*, 124507.

[18] J. E. Lees, A. M. Barnett, D. J. Bassford, R. C. Stevens, A. B. Horsfall, *J. Instrum.* **2011**, *6*, C01032.

[19] G. Bertuccio, S. Caccia, D. Puglisi, D. Macera, *Nucl. Instrum. Methods Phys. Res., Sect. A* **2011**, *652*, 193.

[20] A. M. Barnett, J. E. Lees, D. J. Bassford, J. S. Ng, *Nucl. Instrum. Methods Phys. Res., Sect. A* **2012**, *673*, 10.

[21] S. Butera, G. Lioliou, A. B. Krysa, A. M. Barnett, *J. Appl. Phys.* **2016**, *120*, 024502.

[22] A. Auckloo, J. S. Cheong, X. Meng, C. H. Tan, J. S. Ng, A. Krysa, R. C. Tozer, J. P. R. David, *J. Instrum.* **2016**, *11*, P03021.

[23] G. Lioliou, A. M. Barnett, *Nucl. Instrum. Methods Phys. Res., Sect. A* **2015**, *801*, 63.

[24] A. Owens, *Compound Semiconductor Radiation Detectors*, CRC Press, Florida **2012**.

[25] H. Thiel, M. V. Angel, E. J. Foell, A. L. Rice, G. Schriever, *Environmental Risks from Large-Scale Ecological Research in the Deep Sea–A Desk Study*, European Communities, Luxembourg **1998**.

[26] M. Lück, M. Buscher, H. Lehr, C. Thiede, G. Körner, J. Martin, M. Schlichting, S. Krüger, H. Huthin, in *Proc. IEEE Oceans*, Sydney, **2010**.

[27] R. Pittini, M. Hernes, *Oil Gas Facil.* **2012**, *1*, 47.

[28] P. Kampmann, J. Lemburg, H. Hanff, F. Kirchner, *Hybrid Pressure-Tolerant Electronics*, in *Proc. IEEE Oceans*, Virginia, **2012**.

[29] B. G. Lowe, R. A. Sareen, *Semiconductor X-ray Detectors*, Taylor and Francis Group, Florida **2014**.

[30] M. Bass, *Handbook of Optics: Fundamentals*, 2nd ed., McGraw-Hill, Techniques and Design **1995**.

[31] C. D. Mobley, *Light and Water: Radiative Transfer in Natural Waters*, Academic Press **1994**.

[32] B. L. Henke, E. M. Gullikson, J. C. Davis, *At. Data Nucl. Data Tables* **1993**, *54*, 181.

[33] M. J. S. Belton, K. P. Klaasen, M. C. Clary, J. L. Anderson, C. D. Anger, M. H. Carr, C. R. Chapman, M. E. Davies, R. Greeley, D.

Anderson, L. K. Bolef, T. E. Townsend, R. Greenberg, J. W. Head, G. Neukum, C. B. Pilcher, J. Veverka, P. J. Gierasch, F. P. Fanale, A. P. Ingersoll, H. Masursky, D. Morrison, J. B. Pollack, *Space Sci. Rev.* **1992**, *60*, 413.

[34] M. J. S. Belton, J. W. Head, A. P. Ingersoll, R. Greeley, A. S. McEwen, K. P. Klaasen, D. Senske, R. Pappalardo, G. Collins, A. R. Vasavada, R. Sullivan, D. Simonelli, P. Geissler, M. H. Carr, M. E. Davies, J. Veverka, P. J. Gierasch, D. Banfield, M. Bell, C. R. Chapman, C. Anger, R. Greenberg, G. Neukum, C. B. Pilcher, R. F. Beebe, J. A. Burns, F. Fanale, W. Ip, T. V. Johnson, D. Morrison, J. Moore, G. S. Orton, P. Thomas, R. A. West, *Science* **1996**, *274*, 377.

[35] R. Greenberg, P. Geissler, G. Hoppa, B. R. Tufts, D. D. Durda, R. Pappalardo, J. W. Head, R. Greeley, R. Sullivan, M. H. Carr, *Icarus* **1998**, *135*, 64.

[36] J. M. Moore, E. Asphaug, R. J. Sullivan, J. E. Klemaszewski, K. C. Bender, R. Greeley, P. E. Geissler, A. S. McEwen, E. P. Turtle, C. B. Phillips, B. R. Tufts, J. W. Head, R. T. Pappalardo, K. B. Jones, C. R. Chapman, M. J. S. Belton, R. L. Kirk, D. Morrison, *Icarus* **1998**, *135*, 127.

[37] J. Powell, J. Powell, G. Maise, J. Paniagua, *Acta Astronaut.* **2005**, *57*, 579.

[38] R. E. Thomson, J. R. Delaney, *J. Geophys. Res.-Planet.* **2001**, *106*, 12355.

[39] L. Roth, J. Saur, K. D. Retherford, D. F. Strobel, P. D. Feldman, M. A. McGrath, F. Nimmo, *Science* **2014**, *343*, 171.

[40] W. B. Sparks, K. P. Hand, M. A. McGrath, E. Bergeron, M. Cracraft, S. E. Deustua, *Astrophys. J.* **2016**, *829*, 121.

[41] R. P. Fernandez, A. Sanchez-Torres, *Int. J. Eng. Res. Sci.* **2015**, *1*, 41.

[42] T. Ly Anh, A. Perďochová, V. Nečas, V. Pavlicová, *Nucl. Phys. B-Proc. Sup.* **2006**, *150*, 402.

[43] V. K. Dixit, S. K. Khamari, S. Manwani, S. Porwal, K. Alexander, T. K. Sharma, S. Kher, S. M. Oak, *Nucl. Instrum. Methods Phys. Res., Sect. A* **2015**, *785*, 93.

[44] M. Ladzianský, A. Šagátová, V. Nečas, F. Dubecký, V. Linhart, *Nucl. Instrum. Methods Phys. Res., Sect. A* **2009**, *607*, 135.

[45] A. Šagátová, B. Zaťko, M. Pavlovič, K. Sedlačková, P. Hybler, F. Dubecký, V. Nečas, *J. Instrum.* **2014**, *9*, C04036.

[46] G. Lioliou, A. M. Barnett, *Nucl. Instrum. Methods Phys. Res., Sect. A* **2016**, *836*, 37.

[47] S. M. Sze, K. K. Ng, *Physics of Semiconductor Devices*, John Wiley & Sons, New Jersey **2007**.

[48] G. Bertuccio, R. Casiraghi, *IEEE Trans. Nucl. Sci.* **2003**, *50*, 175.

[49] R. A. Street, *Technology and Applications of Amorphous Silicon*, Springer-Verlag, Berlin **2000**.

[50] M. Mazzillo, A. Sciuto, G. Catania, F. Roccaforte, V. Raineri, *IEEE Sens. J.* **2012**, *12*, 1127.

[51] G. Bertuccio, P. Rehak, D. Xi, *Nucl. Instrum. Methods Phys. Res., Sect. A* **1993**, *326*, 71.

[52] Siliconix, *2N4416/2N4416A/SST4416 N-Channel JFETs*, Vishay Electronic GmbH, Selb, **2001**.

[53] U. Schötzig, *Appl. Radiat. Isot.* **2000**, *53*, 469.

[54] G. W. Fraser, *X-ray detectors in astronomy*, Cambridge University Press, Cambridge **1989**.

[55] G. Bertuccio, D. Maiocchi, *J. Appl. Phys.* **2002**, *92*, 1248.

[56] G. Bertuccio, A. Pullia, J. Lauter, A. Forster, H. Luth, *IEEE Trans. Nucl. Sci.* **1997**, *44*, 1.

[57] G. Bertuccio, A. Pullia, *Rev. Sci. Instrum.* **1993**, *64*, 3294.

[58] G. Bertuccio, *IEEE Solid-State Circuits Mag.* **2012**, *4*, 36.

[59] M. Sánchez del Rio, A. Brunetti, B. Golosio, A. Somogyi, A. Simionovici, European Synchrotron Radiation Facility and University of Sassari, **2003**.

[60] S. Puri, J. S. Shahi, B. Chand, M. L. Garg, N. Singh, P. N. Trehan, N. Nath, *X-Ray Spectrom.* **1998**, *27*, 105.

[61] G. P. Glasby, *Marine Geochemistry*, Springer, Berlin **2006**, 371.

[62] U. Münch, N. Blum, P. Halbach, *Chem. Geol.* **1999**, *155*, 29.

How to cite this article: Lioliou G, Barnett AM. Prototype GaAs X-ray detector and preamplifier electronics for a deep seabed mineral XRF spectrometer. *X-Ray Spectrometry*. 2017;1–14. https://doi.org/10.1002/xrs.2818